A theoretical study of the addition of CH_2OO to hydroxymethyl hydroperoxide and its implications on SO_3 formation in the atmosphere.

Ronald Chow[a] and Daniel K.W. Mok[a,*]

[a] Department of Applied Biology and Chemical Technology, Hong Kong Polytechnic University, Hung Hom, Hong Kong

[*] Corresponding Author, Email: daniel.mok@polyu.edu.hk

Keywords: HMHP; Cregiee Intermediate; Secondary Organic Aerosol; ab initio calculations; TST

Abstract

The reaction of hydroxymethyl hydroperoxide (HMHP, $HOCH_2OOH$) with the simplest Criegee intermediate, CH_2OO, has been examined using quantum chemical methods with transition state theory. Geometry optimization and IRC calculations were performed using M06-2X, MN15-L, and B2PLYP-D3 functionals in conjunction with the aug-cc-pVTZ basis set. Single point energy calculations using QCISD(T) and BD(T) with the same basis set have been performed to determine the energy of reactants, reactive complex, transition state, and products. Rate coefficients have been obtained using variational transition state theory. The addition of CH_2OO on the three different oxygen atoms in HMHP has been considered and the ether oxide forming channel, $CH_2OO + HOCH_2OOH \rightarrow HOCH_2O(O)CH_2OOH$ (channel 2), is the most favorable. The best computed standard enthalpy of reaction (ΔH_{298K}^{RX}) and zero-point corrected barrier height are -20.02 and -6.33 kcal.mol^{-1}, respectively. The reaction barrier is negative and our results suggest that both inner and outer transition states contribute to the corresponding overall reactive flux in the tropospheric temperature range (220 K to 320 K). A two-transition state model has been employed to obtain reliable rate coefficients at the high-pressure limit. The pressure-dependent rate coefficient calculations using the SS-QRRK theory have shown that this channel is pressure-dependent. Moreover, our investigation has shown that the ether oxide formed may rapidly react with SO_2 at 298 K to form SO_3, which can, in turn, react with water to form the atmospheric H_2SO_4. A similar calculation has been conducted for the reaction of HMHP with OH, suggesting the titled reaction may be a significant sink for HMHP. Therefore, the reaction between CH_2OO and $HOCH_2OOH$ could be an indirect source for generating atmospheric H_2SO_4, which is crucial to the formation of clouds, and it might relieve global warming.

Introduction

Organic hydroperoxides have received a lot of attention recently because they may influence the oxidizing capacity of the Earth's atmosphere and the tropospheric budgets of secondary organic aerosols (SOA). They have a longer lifetime in the atmosphere and are less soluble in water than H_2O_2 [1-4], therefore, they can travel over longer distances and distribute the oxidizing radicals OH and HO_2, derived from their photolysis and reactions over a wider area than H_2O_2. They may oxidize SO_2 to produce SO_4^{2-}, deteriorate air quality, and decrease visibility [5, 6]. Sakamoto *et al.* have proposed the possibility of their insertion reaction with other Criegee Intermediates (CIs) to form larger oligomeric hydroperoxides that are more susceptible to deposition into the particle phase, thus contributing to the formation of SOA [7].

Hydroxymethyl hydroperoxide ($HOCH_2OOH$, HMHP) is among the most abundant hydroperoxides observed in the atmosphere as it is the product of the major removal process of the simplest CI, CH_2OO. Alkenes are one of the major volatile organic compounds (VOCs) emitted to the atmosphere. Reaction with ozone is the major sink of alkenes, particularly in highly polluted areas [8], and such reaction will generate CIs. These radicals have high internal energy [9] and can either undergo unimolecular decomposition to form the hydroxyl radical in the atmosphere or undergo collisional relaxation to form stabilized CI (sCI). CH_2OO is the simplest sCI and its reaction with water (or water dimer, more specifically) forms HMHP, which is the major loss process of CH_2OO in atmosphere [9, 10].

The mixing ratio of HMHP varies considerably with locations. The observed concentration typically falls in a low ppbv range during summer and could be up to 5 ppbv over forested regions [11-14]. A field measurement in 2013 across the southeastern United States reported an average mixing ratio of 0.25 ppbv within the boundary layer [15]. The reaction with OH radicals is believed to be the major loss process of HMHP. A theoretical study on the reaction of HMHP and OH has suggested the hydrogen abstraction at the carbon site is the dominant pathway because of the lowest entrance barrier. A barrier height of -0.2 kcal mol^{-1} is obtained for this hydrogen abstraction using CCSD(T)/6-311++G(2df,2p)//MP2/6-31G(d) level of theory [16].

As mentioned earlier, HMHP may also react with sCI to form oligomers. This reaction has been proposed as one of the mechanisms for forming more polar compounds in the atmosphere, contributing to the formation and growth of secondary organic aerosols (SOA) as some of these oligomers have been observed in the SOA collected from the field and generated in laboratory studies. [7, 17-20]. The addition reaction of sCI with HMHP results in oxygenated hydroperoxides, which could further react with other sCI to form oligomeric hydroperoxide, which is more readily transferred to the

condensed phase to contribute to the formation and the growth of secondary aerosols. Thus, the reaction between sCI and $OHCH_2OOH$ would affect the final products during the oxidation of many emitted unsaturated alkenes and a more detailed study would help us to understand the chemistry of CI in the atmosphere.

There are three oxygen atoms in HMHP and CH_2OO may add to each of them results in three addition channels.

$$\mathbf{CH_2OO} + HOCH_2OOH \rightarrow HOCH_2O\mathbf{O}\mathbf{CH_2OO}H \quad (1)$$

$$\mathbf{CH_2OO} + HOCH_2OOH \rightarrow HOCH_2O(O)\mathbf{CH_2OO}H \quad (2)$$

$$\mathbf{CH_2OO} + HOCH_2OOH \rightarrow HOOCH_2O\mathbf{CH_2OO}H \quad (3)$$

Figure 1 illustrated the addition of CH_2OO to different oxygen atoms (color-coded) of HMHP leading to an oligomeric hydroperoxide, an ether oxide, and a dihydroperoxide ether product for channel 1, 2 and 3, respectively. A recent theoretical study on the reaction of sCI and ROOH studied this reaction [21], however, the ether oxide forming channel (channel 2) was not considered. Another study on the reaction between CI and a simpler alkyl hydroperoxide, CH_3OOH, suggested that the ether oxide forming channel may be the most important one [22].

Figure 1 The three reaction channels studied in this work

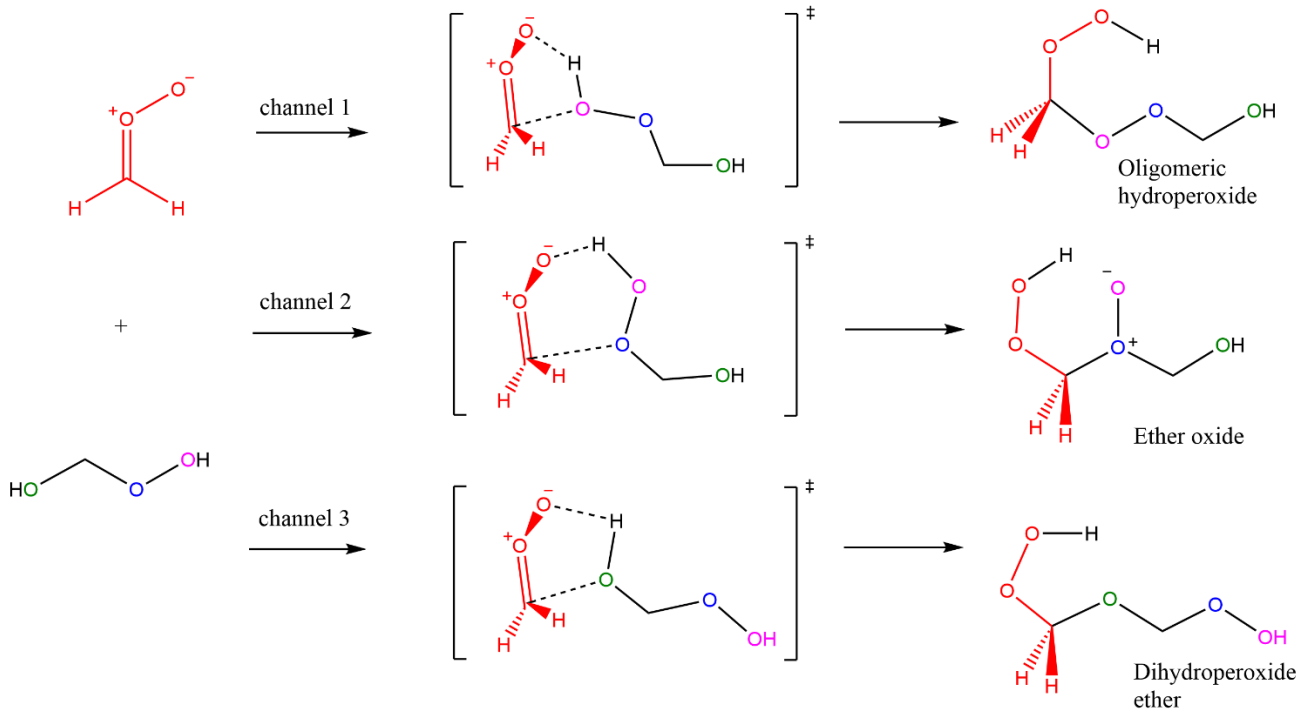

This work aims to investigate all the three possible reaction channels between CH_2OO and $HOCH_2OOH$ and determine theoretical rate coefficients. The results help us to better understand the importance of sCI on the oxidation of $HOCH_2OOH$ and the atmospheric implications of the reaction. The products formed in different channels have entirely different consequences in the atmosphere and understanding their relative importance would certainly be crucial in assessing the significance of this reaction in the oxidation capacity and formation of SOA in the atmosphere.

Methodology

Quantum chemical calculations

Geometry optimizations and vibrational frequencies of reactants, reactive complexes, transition states, and products, were performed using the M06-2X [23], MN-15L [24], and B2PLYP-D3 [25, 26] functionals with the aug-cc-pVDZ (denoted as AVDZ from now on) and the aug-cc-pVTZ level (denoted as AVTZ from now on) basis sets using ultrafine grids. The choice of the density functionals is as follows. The M06-2X functional has been recommended for thermochemistry and kinetic applications and it has been shown to have good performance in obtaining reaction barrier heights [27-31]. The MN15-L functional has been shown to give accurate computed barrier heights of the reaction between Criegee intermediates and water compared to those obtained at the W3X-L//CCSD(T)-F12a/TZ-F12 level [32]. It was chosen because the title reaction was similar to the reaction between Criegee intermediates and water. The B2PLYP-D3 functional has been shown to yield geometries and vibrational frequencies of the stationary points with comparable accuracy to the CCSD(T)/cc-pVTZ level [33, 34]. Although CH_2OO is multi-configurational in nature, previous computational studies have shown that using broken-symmetry unrestricted Kohn-Sham wavefunctions to obtain the ground-state electronic structures of CH_2OO leads to closed-shell wavefunctions [22, 32]. Thus, only single reference quantum chemical methods were employed in this work. QCISD(T) single-point energy calculations were performed to obtain better energy of the stationary point. In some of the stationary points, the T_1 value of CH2OO is larger than 0.022, suggesting the multi-reference character of the species may be important. Thus, the electronic energies of the stationary points were refined using restricted Brueckner doubles with perturbative triple excitation (BD(T)) with the AVTZ basis set. Our previous results have suggested that this approach is effective in obtaining reliable electronic energies for species with some multi-reference character [35]. All DFT, QCISD(T), and BD(T) calculations were performed using Gaussian 16 [36].

Kinetic calculations at the high-pressure limit

After the transition state was located, an intrinsic reaction coordinate calculation was performed for each reaction to confirm that each transition state would lead to the expected reactants and product. All three channels studied in this work have negative barriers. For bimolecular reactions with a negative barrier, there are two transition states in the reaction [37], namely, the outer transition state [37] and the inner transition state (the conventional transition state with one imaginary frequency). The reactive flux will be dominated by the outer transition state at low temperatures and it will be dominated by the inner transition state at high temperatures. At intermediate temperatures, both transition states will contribute to the overall reactive flux. Thus, the overall rate coefficient was calculated according to the two-transition state theory [37]:

$$1/k_{overall} = 1/k_{outer} + 1/k_{inner} \quad (1)$$

The k_{outer} was evaluated using the phase space theory [38], where the two electrically neutral reactants were assumed to interact through a long range attractive effective potential to undergo barrierless association to form a product. The effective potential, V(r), was approximated by $-C_6/r^6 + L^2/(2\mu r^2)$ where C_6 is the $1.5\alpha_1\alpha_2E_1E_2/(E_1+E_2)$, α_i is the polarizability of reactant i (i= 1,2), E_i is the ionization energy of reactant i, r is the separation of the reactants, L is the orbital angular momentum, and μ is the reduced mass of the system [39]. At intermediate L values, the centrifugal barrier arising from the attractive interaction of the two reactants during the association acts as the bottleneck of the reaction. The rate coefficient of the barrierless association reaction at the phase space theory level was then evaluated according to equations 3.1 and 3.3 of reference 38. The isotropic polarizabilities were computed at the MN15-L/AVTZ level because the MN15-L functional had been shown to outperform in computed polarizability values than both M06-2X and B2PLYP functionals [40]. The ionization energies (10.0 eV for CH_2OO [41] and 9.85 eV for $OHCH_2OOH$ [42]) were used in the C_6 potential coefficient calculations.

The k_{inner} was evaluated using different levels of the transition state theory (TST), namely, the conventional transition state theory, the canonical variational transition state theory (CVT), and the improved canonical variational transition state theory (ICVT) with different levels of tunneling corrections, namely small-curvature tunneling (SCT) and zero-curvature tunneling (ZCT) corrections. All levels of TST calculations were performed using PolyRate 2010-A [43]. The relative energies of the IRC points along the minimum energy path (VMEP) at the BD(T)/AVTZ//B2PLYP-D3/AVTZ level were obtained by scaling the VMEP obtained at the B2PLYP-D3/AVTZ level according to reference 44.

Pressure-dependent kinetic calculations

The pressure-dependent rate coefficients were calculated using the system-specific quantum Rice-Ramsperger-Kassel (SS-QRRK) algorithm [45] as implemented in the SS-QRRK utility as part of the POLYRATE 2017 suite [46]. Channels 1 and 2 were treated using the chemical activation mechanism [45]. $k_1(T)$ was computed at the CVT/SCT level. Fitting the forward rate coefficient obtained at the CVT/SCT level using the least square method according to equation 4 in reference [45] gave the parameters (n, E_a, T_0, and A^∞), which were then input into the SS-QRRK program.

The rate coefficients were computed at different pressures (and temperatures) according to the altitudes as described by the US Standard Atmosphere[47]. In the SS-QRRK calculations, pure nitrogen gas used as the bath gas. In this connection, the exponential down model, $\langle\Delta E_{down}\rangle = 200(T/300)^{0.85}$, was used for nitrogen gas as the bath gas in atmospheric modeling [25, 48]. The Lennard-Jones parameters employed in this study were compiled in Table 1. If the experimental Lennard-Jones parameters (σ and ε/k_B) of a compound were not available, their values would be estimated using the Lennard-Jones parameters of a model compound with a similar molecular weight [49]. The values of the model compounds were taken from the manual of MultiWell 2019 [50].

Table 1. The Lennard-Jones parameters of the model compound used for estimating those of CH_2OO and $HOCH_2OOH$.

Compound	Model Compound	σ (Å)	ε/k_B (K)	Reference
CH_2OO	HCOOH	3.79	520	10
$HOCH_2OOH$	C_3H_7OH	4.549	576.7	33
N_2	N/A	3.74	82	33

Results and Discussions

Geometry and Vibration Frequencies of CH_2OO

The geometry of CH_2OO was optimized at the M06-2X/AVXZ (X=D, T), MN15-L/AVXZ, and B2PLYP-D3/AVTZ levels and the rotational constants and vibrational frequencies are shown in Tables S1 and S2, respectively. Since experimental rotational constants and vibrational frequencies were available [32, 51], the theoretical values of the optimized structures of CH_2OO were compared with them. In a previous study of reactions of CH_2OO, Long et al. [32] have also compared the geometries

and vibrational frequencies with these experimental values, some of their values (those obtained at the MN15-L/MG3S and CCSD(T)-F12a/TZ-F12 level) are shown here for comparison. The mean unsigned error (MUE) of the rotational constants between the computed and experimental values (in GHz) is in the following order: CCSD(T)-F12a/TZ-F12 (152.17) [32] < MN15-L/MG3S (878.58) [32] < B2PLYP-D3/AVTZ (969.57) < M06-2X/AVDZ = M06-2X/AVTZ = MN15-L/AVDZ = MN15-L/AVTZ (7479.27). The rotational constants obtained at B2PLYP-D3/AVTZ are very close to those of MN15-L/MG3S. The MUE for vibrational frequencies (in wavenumber) are in the following order: CCSD(T)-F12a/TZ-F12 (19.4) [32] < B2PLYP-D3/AVTZ (43.8) < MN15-L/MG3S (58.4) [32] < MN15-L/AVDZ (62.4) < MN15-L/AVTZ (76.8) < M06-2X/AVTZ (106.2) < M06-2X/AVTZ (112.0). The vibrational frequencies obtained at MN15-L/MG3S in the work of Long and coworkers were scaled by a factor of 0.977.

M06-2X density functional with a basis set of triple-zeta quality is a common approach in studying the reactions of Criegee Intermediates, and the above results suggested that B2PLYP-D3/AVTZ would give better geometries and vibrational frequencies. Since the calculations of the rate coefficients of chemical reactions required the accurate evaluations of rotational and vibrational partition functions, the accuracies in both rotational constants and vibrational frequencies were crucial to the accuracy of the computed rate coefficients of chemical reactions. Thus, the B2PLYP-D3/AVTZ level was chosen as the best lower level method in this study.

Geometries and energies of the reaction profiles

The optimized geometries of the reactant complex (RC), the transition state (TS), and the product (RX) for channels 1, 2, and 3 are shown in Figures S2, S3, and S4, respectively, while those of the reactants are shown in Figure S1. The relative electronic energies of the stationary points determined at different levels of theories are shown in Tables 2-4. Figure 2 depicts the potential energy surfaces (PES) of the three channels at the BD(T)/AVTZ//B2PLYP-D3/AVTZ level which is considered to be the best theoretical estimate in this work. All three channels exhibited a negative barrier and channel 2, the ether oxide forming channel has the lowest reaction barrier while channel 1 is the most exothermic.

Figure 2. Schematic pathways of the three channels (1, 2, and 3) in the CH_2OO + $OHCH_2OOH$ reaction showing the stationary points with their relative electronic energies at 0 K in kcal.mol^{-1} at the BD(T)/AVTZ//B2PLYP-D3/AVTZ level shown in brackets.

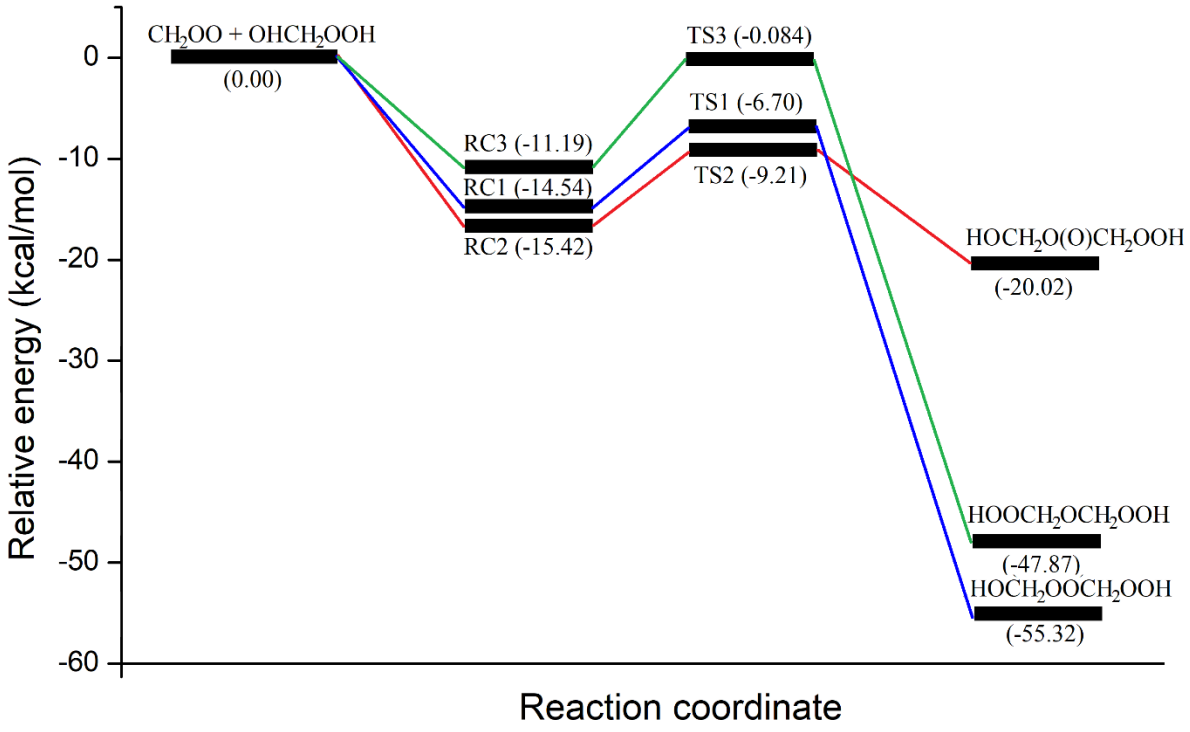

For the DFT results in Tables 2-4, the trend of results from the MN15-L functional seems to be remarkedly different. In Table 2, the barrier height of channel 1 using the M06-2X functional decreases from -7.32 kcal.mol^{-1} with an AVDZ basis set to -8.25 kcal.mol^{-1} with a larger basis set (AVTZ). A similar trend is also observed in Tables 3 and 4 where the barrier height decreases with a more flexible basis set used in the calculation as the transition state would be better described with a larger basis set. Surprisingly, the barrier of channel 1 using the MN15-L functional increases from -6.73 kcal.mol^{-1} to -5.17 kcal.mol^{-1}, using AVDZ and AVTZ respectively, which is not normal. Moreover, the reactant complex optimized at the MN15-L/AVTZ level is different from those obtained at both the M06-2X/AVTZ and B2PLYP-D3/AVTZ levels. MN15-L/AVTZ gives $HOOCH_2O…OCH_2OH$ while the latter two levels suggest $HOCH_2OOH…OOCH_2$ as the reactant complex of this channel (please refer to Figure S2 for details). Therefore, the relative energy results obtained at the MN15-L/AVTZ level might not be reliable.

Table 2. Computed relative energies (kcal.mol^{-1}) of the reactant complex (RC), the transition state (TS) (ΔE(0K) for relative energy of the TS with zero-point correction), separate products (ΔE^{RX}), and the reaction enthalpy at 298 K ($\Delta H_{298K}{}^{RX}$) with respect to separate reactants, of channel 1 $CH_2OO + HOCH_2OOH \rightarrow HOCH_2OOCH_2OOH$ obtained at different levels.

Level	ΔE^{RC}	ΔE^{TS}	ΔE(0K)	ΔE^{RX}	$\Delta H_{298K}{}^{RX}$	Reference
M06-2X/AVDZ	-12.14	-7.32	-5.35	-58.50	-55.68	This work
M06-2X/AVTZ	-16.33	-8.25	-7.08	-59.44	-56.32	This work
MN15-L/AVDZ	-14.58	-6.73	-5.61	-55.05	-52.04	This work
MN15-L/AVTZ	-54.22	-5.17	-4.18	-54.22	-51.21	This work
B2PLYP-D3/AVTZ	-13.41	-6.15	-5.07	-52.16	-49.22	This work
QCISD(T)/AVTZ//M06-2X/AVTZ	-13.93	-5.98	-4.81	-53.57	-50.45	This work
QCISD(T)/AVTZ//MN15-L/AVTZ	-53.68	-5.99	-5.00	-53.68	-50.67	This work
QCISD(T)/AVTZ//B2PLYP-D3/AVTZ	-14.26	-6.19	-5.11	-53.75	-50.81	This work
BD(T)/AVTZ//M06-2X/AVTZ	-14.72	-6.94	-5.77	-55.54	-52.42	This work
BD(T)/AVTZ//MN15-L/AVTZ	-55.267	-6.50	-5.51	-55.27	-52.26	This work
BD(T)/AVTZ//B2PLYP-D3/AVTZ	-14.54	-6.70	-5.62	-55.32	-52.38	This work
M06-2X/def2-TZVP//M06-2X/6-311+G(2df,2p)	-14.3	-6.3		-54.2		6

Table 3. Computed relative energies (kcal.mol^{-1}) of the reactant complex (RC), the transition state (TS) (ΔE(0K) for relative energy of the TS with zero-point correction), separate products (ΔE^{RX}), and the reaction enthalpy at 298 K ($\Delta H_{298K}{}^{RX}$) with respect to separate reactants, of channel 2 $CH_2OO + HOCH_2OOH \rightarrow HOCH_2O(O)CH_2OOH$ obtained at different levels.

Level	ΔE^{RC}	ΔE^{TS}	$\Delta E(0K)$	ΔE^{RX}	$\Delta H_{298K}{}^{RX}$
M06-2X/AVDZ	-16.04	-10.16	-10.34	-22.60	-19.85
M06-2X/AVTZ	-17.21	-11.31	-10.05	-23.76	-20.90
MN15-L/AVTZ	-13.53	-4.91	-4.59	-17.19	-14.38
B2PLYP-D3/AVTZ	-13.91	-7.75	-5.07	-16.46	-13.76
QCISD(T)/AVTZ// M06-2X/AVTZ	-14.74	-7.98	-6.72	-18.50	-15.64
QCISD(T)/AVTZ// MN15-L/AVTZ	-13.43	-7.94	-7.62	-18.52	-15.71
QCISD(T)/AVTZ// B2PLYP-D3/AVTZ	-15.05	-8.14	-5.46	-18.73	-16.03
BD(T)/AVTZ// M06-2X/AVTZ	-15.68	-9.21	-7.95	-20.24	-17.38
BD(T)/AVTZ// MN15-L/AVTZ	-13.69	-8.77	-8.45	-19.85	-17.04
BD(T)/AVTZ// B2PLYP-D3/AVTZ	-15.42	-9.01	-6.33	-20.02	-17.32

Table 4. Computed relative energies (kcal.mol-1) of the reactant complex (RC), the transition state (TS) (ΔE(0K) for relative energy of the TS with zero-point correction), separate products (ΔE^{RX}), and the reaction enthalpy at 298 K ($\Delta H_{298K}{}^{RX}$) with respect to separate reactants, of channel 3 $CH_2OO + HOCH_2OOH \rightarrow HOOCH_2OCH_2OOH$ obtained at different levels.

Level	ΔE^{RC}	ΔE^{TS}	$\Delta E(0K)$	ΔE^{RX}	$\Delta H_{298K}{}^{RX}$	Reference
M06-2X/AVDZ	-58.11	-0.39	-0.67	-50.90	-47.83	This work
M06-2X/AVTZ	-11.47	-1.46	-0.20	-51.78	-48.61	This work
MN15-L/AVTZ	-6.81	2.49	3.46	-45.53	-42.51	This work
B2PLYP-D3/AVTZ	-10.09	0.90	1.84	-44.55	-41.55	This work
QCISD(T)/AVTZ// M06-2X/AVTZ	-9.73	-0.62	0.64	-46.04	-42.87	This work
QCISD(T)/AVTZ// MN15-L/AVTZ	-6.74	0.62	1.59	-46.17	-43.15	This work
QCISD(T)/AVTZ// B2PLYP-D3/AVTZ	-10.88	0.57	1.51	-46.29	-43.29	This work
BD(T)/AVTZ// M06-2X/AVTZ	-10.59	-0.44	0.82	-48.03	-44.86	This work
BD(T)/AVTZ// MN15-L/AVTZ	-6.89	-0.075	0.90	-47.78	-44.76	This work
BD(T)/AVTZ// B2PLYP-D3/AVTZ	-11.19	-0.084	0.86	-47.87	-44.87	This work
M06-2X/def2-TZVP//M06-2X/6-311+G(2df,2p)	-13.9	-2.0		-52.7		6

The T_1 diagnostics of the QCISD(T)/AVTZ calculations using optimized geometries at M06-2X/AVTZ, MN15-L/AVTZ, and B2PLYP-D3/AVTZ of the stationary points of the three channels are shown in Table 5. A T_1 diagnostic of less than 0.022 for a closed-shell species [52] suggests the multi-reference character of the state should not have a significant effect on the results. The T_1 values in the QCISD(T)/AVTZ results of CH_2OO are, as expected, rather large (0.055 – 0.058). Yet, the T_1 values of the reactant complex and the transition state are decreasing, suggesting the multi-reference effects on the results would be small. Thus, Brueckner doubles with perturbative triple excitation (BD(T)) have been employed to refine the electronic energies of the stationary points. From the T_1 diagnostic values, we believe the approach adopted in this study would be adequate to describe the stationary points along the reaction potential energy surface.

Table 5. T_1 diagnostics of the stationary points of the three channels computed at the QCISD(T)/AVTZ level using geometries optimized at different DFT levels.

Channel 1: $CH_2OO + HOCH_2OOH \rightarrow HOCH_2OOCH_2OOH$					
Geometry	CH_2OO	$HOCH_2OOH$	RC	TS	Product
M06-2X/AVTZ	0.055	0.014	0.031	0.027	0.015
MN15-L/AVTZ	0.058	0.014	0.015	0.028	0.015
B2PLYP-D3/AVTZ	0.058	0.014	0.033	0.028	0.015
Channel 2: $CH_2OO + HOCH_2OOH \rightarrow HOCH_2O(O)CH_2OOH$					
Geometry			RC	TS	Product
M06-2X/AVTZ			0.029	0.023	0.017
MN15-L/AVTZ			0.034	0.023	0.017
B2PLYP-D3/AVTZ			0.032	0.022	0.018
Channel 3: $CH_2OO + HOCH_2OOH \rightarrow HOOCH_2OCH_2OOH$					
Geometry			RC	TS	Product
M06-2X/AVTZ			0.030	0.026	0.014
MN15-L/AVTZ			0.035	0.025	0.014
B2PLYP-D3/AVTZ			0.032	0.026	0.014

The relative energy of a stationary point computed at the BD(T)/AVTZ level is lower than that of the same stationary point computed at the QCISD(T)/AVTZ level for all the three channels. Taking channel 1 as an example (Table 2), the differences in the computed barrier heights using the same geometry between the BD(T)/AVTZ level and the QCISD(T)/AVTZ level are -0.96, -0.51, and -0.51 kcal.mol^{-1} for the geometries optimized at the M06-2X/AVTZ, MN15-L/AVTZ, and B2PLYP-D3/AVTZ level, respectively. At 298 K, the reduction of the computed barrier height by 1 kcal.mol^{-1} leads to an increase by a factor of 5.4 in the computed rate coefficients at the TST level. This shows the importance of obtaining accurate barrier heights in the determination of reliable rate coefficients.

Comparisons with previous studies

Chen and coworkers performed extensive calculations on the reactions between sCIs and ROOH, including channels 1 and 3 in this work, at the M06-2X/def2-TZVP//M06-2X/6-311+G(2df,2p) level of theory. For channel 1, the best computed barrier height and the best computed reaction energy of this work agree very well with those of their work (see Table 2). For channel 3, the best computed reaction energy in this work is higher than that computed by Chen and coworkers by 4.83 kcal.mol^{-1}. The discrepancies are likely to arise as only the DFT method has been employed in Chen's study[21].

The BD(T) single-point energies would give a better estimate of the energetics of the reaction. The reaction enthalpy obtained is -44.87 kcal.mol^{-1} and its zero-point corrected barrier height is 0.86 kcal.mol^{-1} at the BD(T)/AVTZ//B2PLYP-D3/AVTZ level.

Vereecken et al [18] reported the reaction between the simplest Criegee intermediate (CH_2OO) and methyl hydroperoxide (CH_3OOH). Two significant differences in the reaction pathways were observed. First, although there were two channels, the $CH_2OO + CH_3OOH \rightarrow CH_3OOCH_2OOH$ channel (which is analogous to channel 1 in this work), and the $CH_2OO + CH_3OOH \rightarrow CH_3O(O)CH_2OOH$ (which is analogous to channel 2 in this work) which proceeded through different transition states, they shared the same reactant complex. However, in the reaction between CH_2OO and HMHP, these two channels had different reactant complexes, even though M06-2X/AVTZ was used in both this study and Vereecken's work. The computed barrier height of the two aforementioned channels at CCSD(T)/AVTZ//M06-2X/AVTZ in the work of Vereecken and coworkers was 1.7 kcal.mol^{-1} , which was smaller than the difference in barrier heights between channel 1 and channel 2 in this study (2.28 kcal.mol^{-1}) at BD(T)/AVTZ//M06-2X/AVTZ level. Thus, the reaction rates of channels 1 and 2 in this work were not expected to be comparable. Detailed kinetic studies on channels 1 and 2 would be discussed in the next section. The ether oxide channel (channel 2) which was missing in the theoretical study on the same reaction between CH_2OO and HMHP reported before[53], turned out to be the most favorable channel of the reaction.

The most accurate method in this work is the BD(T)/AVTZ//B2PLYP-D3/AVTZ level, which gives the computed barrier heights of -6.70 kcal.mol-1, -9.01 kcal.mol-1 and -0.084 kcal.mol-1 for channel 1, 2 and 3, respectively. In terms of reaction energy, the computed reaction energies (ΔE^{RX}) at the same level were in the order: channel 2 (-20.02 kcal.mol-1) > channel 3 (-47.87 kcal.mol-1) > channel 1 (-55.32 kcal.mol-1), therefore, the oligomeric hydroperoxide forming channel is the most exothermic while the ether oxide forming channel is the most favorable.

Rate coefficient results

As the barrier height of channel 3 is positive while channels 1 and 2 proceed through a negative barrier, rate coefficient calculations were only performed on channels 1 and 2 in the temperature range of 200 – 400 K. For bimolecular reactions with a negative barrier, both the outer and inner transition states may contribute to the overall rate coefficient ($k_{overall}$). The $k_{overall}$ was determined using equation (1) while k_{outer} was computed using the phase space theory and k_{inner} was computed using different TST

levels using the minimum energy paths (MEPs) obtained at the BD(T)/AVTZ//B2PLYP-D3/AVTZ level.

Figure 3 *VMEP*, ΔZPE and ΔV_a^G curves of channel 1 $CH_2OO + HOCH_2OOH \rightarrow HOCH_2OOCH_2OOH$ from POLYRATE calculations at the BD(T)/AVTZ//B2PLYP-D3/AVTZ level (energies with respect to separate reactants).

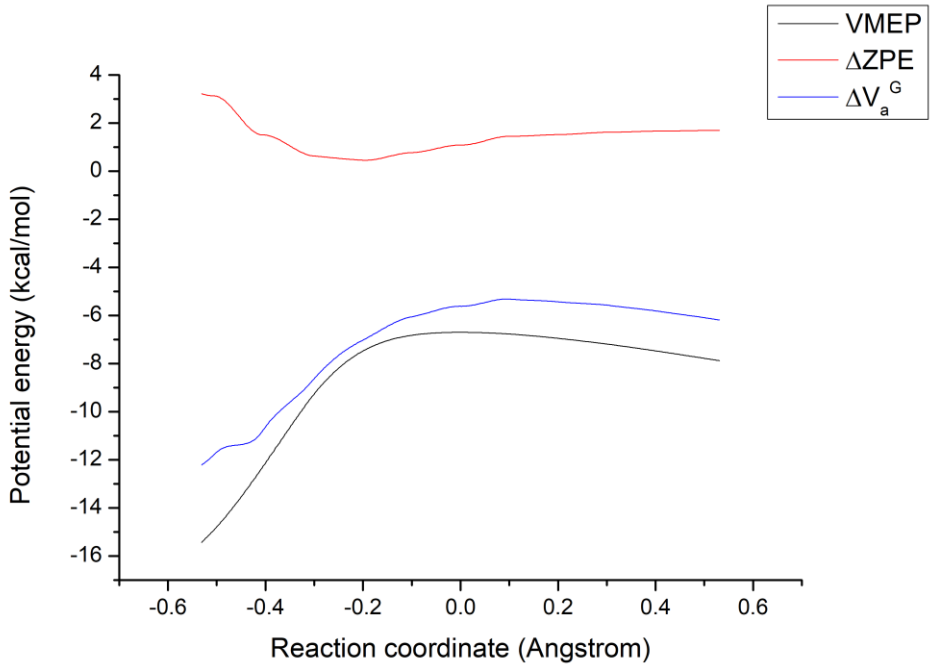

The classical potential energy curve (*VMEP*), the zero-point energy difference curve (ΔZPE), and the ground-state vibrationally adiabatic energy difference curve (ΔV_a^G = *VMEP* + ΔZPE, where ΔZPE is the difference in zero-point energy between an IRC point and the sum of reactants) of channels 1 and 2 are shown in Figures 3 and S6, respectively. A dip is observed in each ΔZPE curve in these two figures, which is caused by bond-forming and bond-breaking processes along the reaction coordinate. The dips of the two ΔZPE curves are located *s* = -0.195 Å and -0.15 Å in channels 1 and 2, respectively. The shape of the ΔV_a^G curve is given by combining the *VMEP* and the ΔZPE curves. The maxima of the ΔV_a^G curves (denoted as ΔV_a^G(s*)) occur at *s* = 0.095 and 0.230 Å for channels 1 and 2, respectively. The deviation of the maximum of the ΔV_a^G curve from s = 0 Å suggests that the classical transmission

coefficient (known as CAG factor and denoted as κ^{CAG}) is significant. In variation TST theory, the rate coefficient is given by

$$k(\text{with tunneling}) = \kappa^{CAG} \times \kappa(\text{tunneling}) \times k(\text{without tunneling}) \quad (3)$$

The computed values of $\kappa^{TST/CAG}$, $\kappa^{CVT/CAG}$, and the tunneling correction factors for channels 1 and 2 are tabulated in Tables S3 and S6 (in the supplementary material), respectively. For both channels, tunneling is negligible ($\kappa^{ZCT} = \kappa^{SCT} = 1$) in the temperature range considered. The κ^{CAG} at TST and CVT levels are given by $\kappa^{TST/CAG} = \exp[(\Delta V_a^G(s=0) - \Delta V_a^G(s^*))/RT]$ and $\kappa^{CVT/CAG} = \exp[(\Delta V_a^G(s^{*CVT(T)}) - \Delta V_a^G(s^*))/RT]$, respectively [54, 55]. At the ICVT level, since the dividing surface of the generalized transition state is defined at the maximum of the V_a^G curve, there is no CAG correction factor.

For channel 1, Table S3 shows that the $\kappa^{TST/CAG}$ values range from 0.468 at 200 K to 0.684 at 400 K. Throughout the temperature range considered, the $\kappa^{TST/CAG}$ values are much smaller than 1, indicating that there are significant recrossing trajectories [56]. Thus, the variational transition state theory (VTST) is required to obtain accurate rate coefficients due to the heavy recrossing effect. $\kappa^{TST/CAG}$ in channel 2 ranges from 0.3033 at 200 K to 0.5507 at 400 K, so the variational transition state theory is required to obtain accurate rate coefficients for channel 2.

The computed rate coefficients (with and without tunneling corrections) for channels 1 and 2 are tabulated in Tables S4 and S7, respectively. Since κ^{ZCT} is the same as κ^{SCT} at 200 – 400 K, $k^{TST/ZCT}$, $k^{CVT/ZCT}$, and $k^{ICVT/ZCT}$ are not listed in the tables because they are the same as their SCT counterparts. The computed k versus T plot and the $\log_{10} k$ Vs $1000/T$ plot for channels 1 and 2 are shown in Figures 4a and Figure 5a, respectively, where a negative temperature dependence is clearly observed for the computed rate coefficients at all TST levels for both channels.

To investigate the effects of the outer and the inner transition states on the overall rate coefficients, two-transition state theory calculations were carried out for both channels. The computed k_{outer}, k_{inner} (the same as k^{ICVT}), and the $k_{overall}$ versus temperature for channels 1 and 2 are shown in Figures 4b and 5b, respectively, and their values are compiled in Tables S5 and S8, respectively. In channel 1, the results show that the outer transition state dominates the overall reactive flux at $T < 220$ K while the inner transition state dominates the overall reactive flux at $T \geq 260$ K. At the intermediate temperature range (220 – 260 K), both the outer and the inner transition states contribute to the overall reactive flux of the reaction. In channel 2, Figure 5b shows that the $k_{overall}$ is dominated by k_{outer} from 200 – 250 K, so the overall reactive flux of this reaction is dominated by the outer transition state at

low temperatures (200 – 270 K). Table S8 shows that at intermediate temperatures (280 – 330 K), both outer and inner transition states contribute to the overall reactive flux. The inner transition state dominates the reactive flux at T ≥ 340 K.

To examine the pressure dependence of the computed rate coefficients, SS-QRRK calculations were performed for both channels at specific atmospheric conditions to reflect the actual temperature and pressure values at different altitudes in the troposphere. The computed SS-QRRK values are compiled in Tables S9. The results show that channel 1 is independent of pressure while channel 2 is pressure dependent. The ether oxide is expected to be produced at the highest rate at an elevation of 12 km, corresponding to the temperature of 217 K and the pressure of 1.940×10^4 Pa.

Figure 4 (a) Computed (BD(T)/AVTZ//B2PLYP-D3/AVTZ) k (cm^3 $molecule^{-1}s^{-1}$) versus T(K) curves (upper) and $\log_{10}k$ versus 1000/T curves (lower) channel 1 $CH_2OO + HOCH_2OOH \rightarrow HOCH_2OOCH_2OOH$ obtained at TST (TST, TST/ZCT, and TST/SCT) and various VTST levels (CVT, ICVT, CVT/ZCT, CVT/SCT, ICVT/ZCT, and ICVT/SCT) using POLYRATE. As $k^{CVT} \sim= k^{ICVT}$ and $\kappa^{ZCT} = \kappa^{SCT} = 1$, k^{CVT}, k^{ICVT}, $k^{CVT/ZCT}$, $k^{ICVT/ZCT}$, $k^{CVT/SCT}$ and $k^{ICVT/SCT}$ curves overlap with each other. Also, since $k^{TST/SCT} = k^{TST/ZCT}$, they overlap with each other. (b) Computed k_{outer}, k_{inner}, and $k_{overall}$ (cm^3 $molecule^{-1}s^{-1}$) versus T(K) curves of the channel 1 $CH_2OO + HOCH_2OOH \rightarrow HOCH_2OOCH_2OOH$. k_{outer} and k_{inner} were evaluated at the PST and the ICVT levels, respectively and $k_{overall}$ was calculated using equation 1.

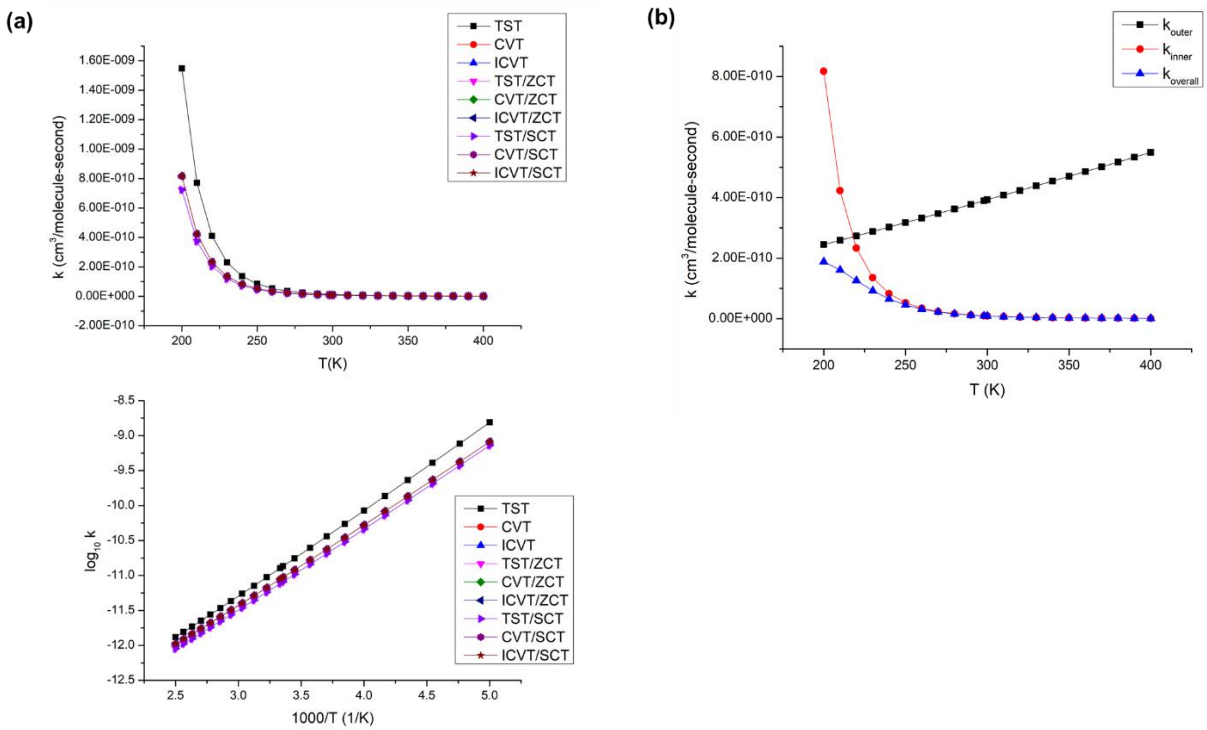

Figure 5(a) Computed (BD(T)/AVTZ//B2PLYP-D3/AVTZ) k (cm^3 $molecule^{-1}s^{-1}$) versus T(K) curves (upper) and $\log_{10}k$ versus $1000/T$ curves (lower) of channel 2 CH_2OO + $HOCH_2OOH$ → $HOCH_2O(O)CH_2OOH$ obtained at TST (TST, TST/ZCT, and TST/SCT) and various VTST levels (CVT, ICVT, CVT/ZCT, CVT/SCT, ICVT/ZCT, and ICVT/SCT) using POLYRATE. As k^{CVT} ~= k^{ICVT} and $\kappa^{ZCT} = \kappa^{SCT} = 1$, k^{CVT}, k^{ICVT}, $k^{CVT/ZCT}$, $k^{ICVT/ZCT}$, $k^{CVT/SCT}$ and $k^{ICVT/SCT}$ curves overlap with each other. Also, since $k^{TST/SCT} = k^{TST/ZCT}$, they overlap with each other. (b) Computed k_{outer} (black), k_{inner} (red), and $k_{overall}$ (blue) (cm^3 $molecule^{-1}s^{-1}$) versus T(K) curves of the channel 2 CH_2OO + $HOCH_2OOH$ → $HOCH_2O(O)CH_2OOH$. k_{outer} and k_{inner} were evaluated at the PST and the ICVT levels, respectively and $k_{overall}$ was calculated using equation 1.

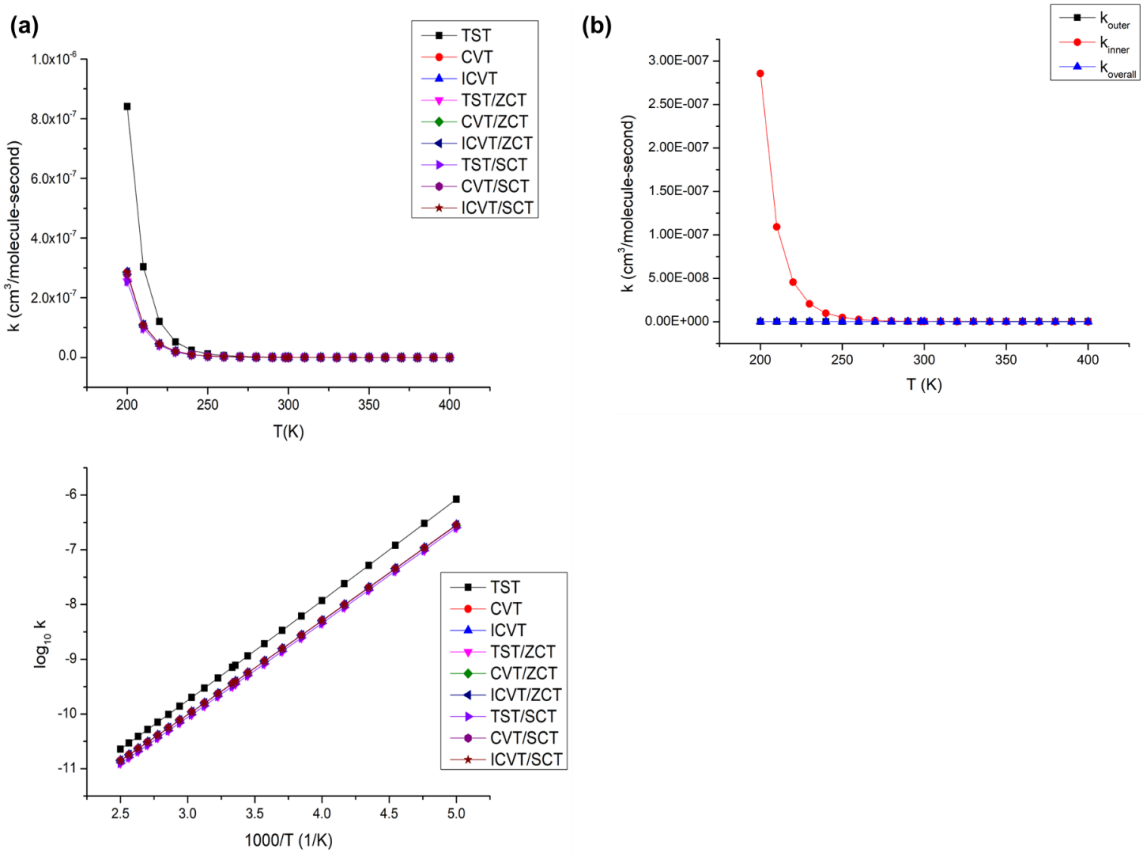

Chen and coworkers [21] carried out the calculation of the rate coefficient for the oligomeric hydroperoxide forming channel (channel 1) from 273 K to 400 K at the TST level using the relative energies obtained at the M06-2X/def2-TZVP//M06-2X/6-311G(2df,2p) level. The rate coefficients are in excellent agreement with the results obtained here using B2PLYP-D3/AVTZ although the effect of the outer transition state on the overall flux of the reaction was not considered. From our results, the outer transition state becomes a more and more important bottleneck and has to be taken into consideration in order to get a good estimate of the reactive flux and the rate coefficients at T ≤ 260 K. For bimolecular reactions with a negative barrier, the k_{inner} has a negative temperature dependency, thus the k_{inner} become closer to k_{outer} as temperature increases. The contributions of the two bottlenecks

(the inner and the outer transition state) become comparable. Moreover, employing the TST method cannot give reliable rate coefficients at T ≤ 270 K because of the large variational effect of the computed *k*, which means that the rate coefficients are not computed using the correct barrier height of the reaction using TST. Perhaps, these are the reasons why the author only computed rate coefficients at higher temperatures.

Atmospheric Implications

Kinetic calculations have been performed for two of the channels in this work, namely, the oligomeric hydroperoxide forming channel (i.e. channel 1) and the ether oxide forming channel (i.e. channel 2). Figure 6 shows the computed $k_{overall}$ values of these two channels versus temperature. As mentioned before, $k_{overall}$ is dominated by k_{outer} (evaluated at the PST level) from 200 K to 250 K. In PST, the rate coefficient of the barrierless association reaction is proportional to $T^{1/6}$, so the computed $k_{overall}$ values of channel 2 increase from 200 K to 250 K. At $T > 250$ K, the k_{inner} of channel 2 (evaluated at the ICVT level), which has negative temperature dependence, starts to dominate the $k_{overall}$ values. Thus, the $k_{overall}$ values decrease from 250 K to 400 K, leading to the wavy appearance of the $k_{overall}$ versus *T* curve for channel 2.

Figure 6 Computed (BD(T)/AVTZ//B2PLYP-D3/AVTZ) $k_{overall}$ (cm^3 $molecule^{-1}$ $second^{-1}$) of channels 1 ($CH_2OO + HOCH_2OOH \rightarrow HOCH_2OOCH_2OOH$) and 2 ($CH_2OO + HOCH_2OOH \rightarrow HOCH_2O(O)CH_2OOH$) using two-transition state theory.

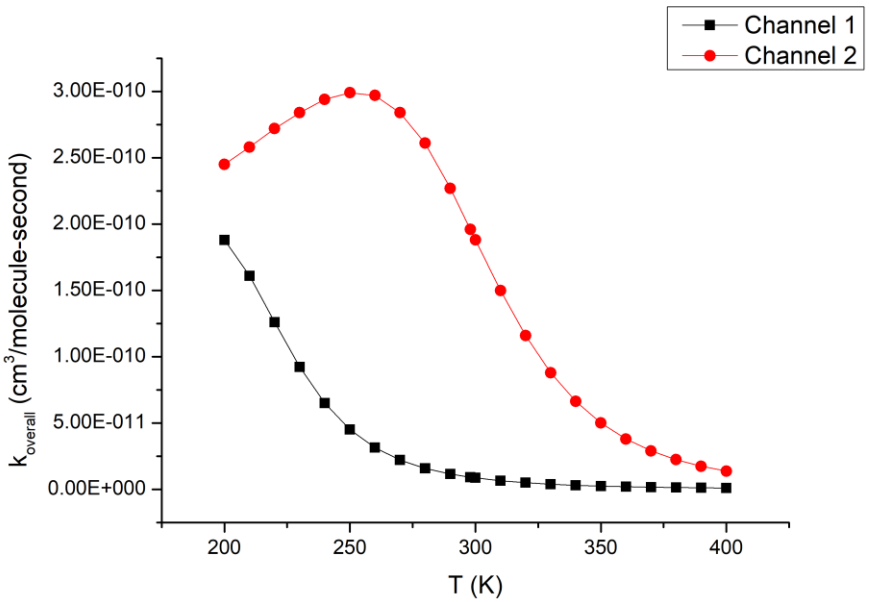

In general, the $k_{overall}$ of channel 2 is greater than that of channel 1 at the same temperature from 200 K to 400 K, as shown in Figure 6. Therefore, the generation of the ether oxide product is faster than that of the oligomeric hydroperoxide product from the $OHCH_2OOH + CH_2OO$ reaction in the temperature range considered. By taking the ratio of k_2/k_1 (compiled in Table S10), where k_2 is the $k_{overall}$ of channel 2 and k_1 is the $k_{overall}$ of channel 1, one can quantify the difference in the production rate of the two species at different temperatures. In the troposphere, where the temperature ranges from 210 K to 320 K, the production rate of the ether oxide product is higher than that of the oligomeric hydroperoxide product by a factor of 1.6 (at 210 K) to 22.8 (at 320 K). Under normal atmospheric conditions, the production rate of the ether oxide product is at least 10 times more

As shown in Figure 2, although the transition state of channel 2 is the lowest in energy among the three channels studied, the ether oxide product formed is about 30 kcal/mol higher in energy than the other two hydroperoxide products. It is more reactive and may react with the more abundant species in the atmosphere, such as water and sulfur dioxide. Studies on the reactions of ether oxide are relatively rare. Vereecken et al. performed calculations to examine the reaction of the ether oxide from the reaction between the CH_3OOH and CH_2OO [22] and concluded that it is not reactive towards water. They also examined the possibility of the ether oxide reacting with SO_2 and concluded that the reaction might only be important in areas with a high concentration of SO_2 as the rate coefficient at the TST level was rather slow (2×10^{-13} $cm^3molecule^{-1}second^{-1}$) at 298K. The reaction $HOCH_2O(O)CH_2OOH + SO_2 \rightarrow HOCH_2OCH_2OOH + SO_3$ has been examined to see whether it is a possible sink of HMHP.

In view of the large size of this reacting system, geometry optimizations of the stationary points were performed at the M06-2X/AVDZ level only and the electronic energies were refined at the BD(T)/AVTZ level. The potential energy surface of this reaction obtained at the BD(T)/AVTZ//M06-2X/AVDZ level showed that the two reactants underwent barrierless association to form a reactant complex, with stabilization energy of 12.07 $kcal.mol^{-1}$ (at the BD(T)/AVTZ//M06-2X/AVDZ level), then the reaction proceeded via a submerged barrier of -8.13 $kcal.mol^{-1}$. It then proceeded to form a product complex with relative electronic energy of -81.27 $kcal.mol^{-1}$ and finally, it dissociated to form separate products with reaction energy of -64.35 $kcal.mol^{-1}$. The reaction between $HOCH_2O(O)CH_2OOH$ and SO_2 was a very exothermic reaction with a very negative barrier height. To obtain reliable rate coefficients for this reaction, the two-transition state theory was employed to compute the rate coefficients from 200 K to 400 K. However, since the experimental ionization energy of ether oxide, $HOCH_2O(O)CH_2OOH$, was not available, the k_{outer} at the PST level could not be calculated accurately. Regarding k_{inner}, in view of the high computational costs of the Hessians of the reacting system along the IRC, k_{inner} was only computed at the TST level and the results are compiled

in Table S11. At 298 K, the computed rate coefficient of the $HOCH_2O(O)CH_2OOH + SO_2 \rightarrow HOCH_2OCH_2OOH + SO_3$ reaction was 5.15 x 10^{-10} $cm^3molecule^{-1}second^{-1}$ at the TST level, which was three orders of magnitude greater than that of the $HOOCH_2O(O)CH_3 + SO_2 \rightarrow HOOCH_2OCH_3 + SO_3$ reaction at the TST level. Although the TST rate coefficient might be overestimated by an order of magnitude, our results still suggest that HMHP reaction with CI may result in oxidizing of SO_2 into SO_3. Thus, the title reaction may be a source of H_2SO_4, which facilitates the production of clouds, leading to a relief of global warming [57].

In order to further understand the potential of HMHP in the production of SO_3, we tried to compare the rate of titled reaction with that of the reaction with OH, the reaction that had been thought to be the major loss pathway of HMHP in the atmosphere. There was a theoretical study on the reaction of HMHP with OH using CCSD(T)/6-311++G(2df,2p)//MP2/6-31G(d) level of theory [16]. In that study, hydrogen abstraction from the OH, OOH, and the CH_2 group was examined. The channel with the lowest barrier height was hydrogen abstraction from the CH_2 group which was slightly negative (-0.2 $kcal.mol^{-1}$). The barrier height was quite high compared with that of the reaction between HMHP and CH_2OO in the current study. There were reports suggesting that MP2 tends to overestimate barrier heights of gas-phase hydrogen abstraction reactions [58]. Moreover, the 6-31G(d) basis set lacks diffuse functions and may not be sufficient in locating the accurate transition state structure and barrier heights [59]. Thus, BD(T)/AVTZ//M06-2X/AVTZ calculations were conducted to obtain the stationary points structures and energies for the hydrogen abstraction of OH from the CH_2 group of HMHP (which has been concluded as the most favorable channel [58]). Surprisingly, the barrier height obtained is -1.77 $kcal.mol^{-1}$ which agrees reasonably well with the value reported previously. The kinetic calculation was performed to obtain the k_{inner} and the results can be found in Table S12 of the supplemental material. At 298K, the k_{inner} is 6.90 x 10^{-13} $cm^3molecule^{-1}second^{-1}$ at the ICVT level. The k_{inner} is very small compared with k_{outer} (3.81 x 10^{-9} $cm^3molecule^{-1}second^{-1}$), so $k_{overall}$ basically equals to k_{inner}. Thus, the reaction of HMHP with sCI (CH_2OO) would be about 300-fold faster than that with OH.

The concentration of OH is typically around 1×10^6 molecules cm^{-3} and peak concentration could be more than twice of that [60]. The concentration of sCI in the atmosphere has not been determined reliably. A modelling study suggested that the peak concentration of sCI was at a level of 1×10^5 molecules cm^{-3}. A study based on field data and reaction model estimated the average concentration of sCI in boreal forests and rural environments of Finland and Germany was at a level of 5.0×10^4 molecules cm^{-3} (with an order of magnitude uncertainty) [61]. Another similar study in urban and urban sites in the UK suggested a lower average sCI concentration of 30 – 3000 molecules cm^{-3} with about 13% accounted by CH_2OO [62]. Since HMHP is a product of CH_2OO reacting with water (dimer), one

could safely assume that in areas where HMHP content is high, the concentration of CH_2OO would be at the high side as well. Assuming 13% of sCI are CH_2OO, the concentration of CH_2OO could be about 5.0×10^3 molecules cm^{-3}. Thus, the concentration of OH is about 200-fold higher than that of CH_2OO, and the rate of HMHP with OH is 300-fold slower. From this point of view, the reaction CH_2OO could be a competitive reaction partner and OH may not be the only major loss process of HMHP.

For sCI like CH_2OO, unimolecular decay is responsible for just over half of the loss. Besides its reaction with water vapor being the major loss pathway, the remaining loss pathways would give HMHP. From this perspective, CH_2OO would be an important partner of HMHP in the rural area leading to an ether oxide product, which could oxidize SO_2 into SO_3. Although reactions of sCI with SO_2 have a negligible impact on the global gas phase H_2SO_4, the titled reaction may provide an indirect pathway for CH_2OO to contribute to the formation of gas-phase H_2SO_4.

Conclusion

The addition of CH_2OO to the three different oxygen atoms on $HOCH_2OOH$ has been investigated computationally using density functionals (M06-2X, MN15-L, and B2PLYP-D3) and high-level *ab initio* methods (QCISD(T) and BD(T)). The B2PLYP-D3 functional is found to outperform the M06-2X and the MN15-L functionals in geometry optimization and it has been used to obtain the geometry of all the stationary points in this study. Channel 2, the addition channel forming an ether oxide, $CH_2OO + HOCH_2OOH \rightarrow HOCH_2O(O)CH_2OOH$, is found to have the smallest barrier. This channel has not been considered in a recent theoretical study of the same reaction.

All the channels have a negative barrier and two transition state theory has been used to obtain the rate coefficients. For the major channel, the two-transition state theory calculation shows that the outer transition state dominates the overall reactive flux below 270 K while both outer and inner transition states become important from 270 K to 330 K. Thus, it is crucial to account for the contributions from the two transition states to the overall reactive flux to obtain reliable rate coefficients at the tropospheric temperature range (220 – 320 K). Furthermore, the pressure-dependent behaviour of the rate coefficients of this channel was also investigated using the SS-QRRK method from 200 K to 400 K. The SS-QRRK rate coefficients show the expected behaviour of the falloff curves in the temperature range considered. The rate of channel 2 is an order of magnitude faster than that of channel 1.

Extended calculations have shown that the reaction between $HOCH_2O(O)CH_2OOH$ (a hydroxy-substituted ether oxide) and SO_2 proceeds quickly with the rate constant of 5.15×10^{-10} $cm^3molecule^{-1}second^{-1}$ at 298 K. Thus, the major channel of the titled reaction, $CH_2OO + HOCH_2OOH \rightarrow HOCH_2O(O)CH_2OOH$, could be responsible for the production of SO_3 in the troposphere. We have also calculated the overall reaction rate of HMHP with OH using BD(T)//M06-2X/AVTZ and obtained a rate coefficient about 300-fold smaller than the reaction. Our results suggest that the titled reaction may provide an indirect way for sCI to contribute to the production of SO_3. Since SO_3 reacts with H_2O to form H_2SO_4, which plays the role of a nucleating agent in the atmosphere, the formation of clouds could be facilitated by this process. Thus, the major channel of the titled reaction could promote the formation of clouds in the atmosphere, leading to an overall reduction in the temperature of the Earth's surface, thereby relieving global warming.

Conflicts of interest

There are no conflicts to declare.

Acknowledgements

The authors are grateful to the Research Grant Council (RGC) of the Hong Kong Special Administrative Region (Grant Number: PolyU 150313/15P), and the Research Committee of the Hong Kong Polytechnic University (Account No. A-PK41 and G-YBAV) for their funding support.

Reference

1. D. S. Cohan, M. G. Schultz, D. J. Jacob, B. G. Heikes and D. R. Blake, *J. Geophys. Res.*, 1999, **104**, 5717-5724.
2. C. X. Wang and Z. M. Chen, *Prog Nat Sci*, 2006, **16**, 1141-1149.
3. L. Jaegle, D. J. Jacob, P. O. Wennberg, C. M. Spivakovsky, T. F. Hanisco, E. J. Lanzendorf, E. J. Hintsa, D. W. Fahey, E. R. Keim, M. H. Proffitt, E. L. Atlas, F. Flocke, S. Schauffler, C. T. McElroy, C. Midwinter, L. Pfister and J. C. Wilson, *Geophys. Res. Letts.*, 1997, **24**, 3181-3184.
4. F. Ravetta, D. J. Jacob, W. H. Brune, B. G. Heikes, B. E. Anderson, D. R. Blake, G. L. Gregory, G. W. Sachse, S. T. Sandholm, R. E. Shetter, H. B. Singh and R. W. Talbot, *J. Geophys. Res.*, 2001, **106**, 32709-32716.
5. J. A. Lind, A. L. Lazrus and G. L. Kok, *J. Geophys. Res.: Atmos.*, 1987, **92**, 4171-4177.
6. X. Zhou and Y. N. Lee, *J. Phys. Chem.*, 1992, **96**, 265-272.
7. Y. Sakamoto, S. Inomata and J. Hirokawa, *J. Phys. Chem. A*, 2013, **117**, 12912-12921.
8. M. A. H. Khan, C. J. Percival, R. L. Caravan, C. A. Taatjes and D. E. Shallcross, *Environ. Sci.: Processes Impacts*, 2018, **20**, 437-453.
9. D. Johnson and G. Marston, *Chemical Society Reviews*, 2008, **37**, 699-716.

10. L. Sheps, B. Rotavera, A. J. Eskola, D. L. Osborn, C. A. Taatjes, K. Au, D. E. Shallcross, M. A. H. Khan and C. J. Percival, *Physical Chemistry Chemical Physics*, 2017, **19**, 21970-21979.
11. M. Fels and W. Junkermann, *Geophys. Res. Lett.*, 1994, **21**, 341-344.
12. J. H. Lee, D. F. Leahy, I. N. Tang and L. Newman, *J. Geophys. Res.: Atmos.*, 1993, **98**, 2911-2915.
13. T. B. Nguyen, J. D. Crounse, A. P. Teng, J. M. St. Clair, F. Paulot, G. M. Wolfe and P. O. Wennberg, *Proc. Natl. Acad. Sci.*, 2015, **112**, E392-E401.
14. J. B. Weinstein-Lloyd, J. H. Lee, P. H. Daum, L. I. Kleinman, L. J. Nunnermacker, S. R. Springston and L. Newman, *J. Geophys. Res.: Atmos.*, 1998, **103**, 22361-22373.
15. H. M. Allen, J. D. Crounse, K. H. Bates, A. P. Teng, M. P. Krawiec-Thayer, J. C. Rivera-Rios, F. N. Keutsch, J. M. St Clair, T. F. Hanisco, K. H. Moller, H. G. Kjaergaard and P. O. Wennberg, *J. Phys. Chem. A*, 2018, **122**, 6292-6302.
16. J. S. Francisco and W. Eisfeld, *J. Phys. Chem. A*, 2009, **113**, 7593-7600.
17. M. Hallquist, J. C. Wenger, U. Baltensperger, Y. Rudich, D. Simpson, M. Claeys, J. Dommen, N. M. Donahue, C. George, A. H. Goldstein, J. F. Hamilton, H. Herrmann, T. Hoffmann, Y. Iinuma, M. Jang, M. E. Jenkin, J. L. Jimenez, A. Kiendler-Scharr, W. Maenhaut, G. McFiggans, T. F. Mentel, A. Monod, A. S. H. Prévôt, J. H. Seinfeld, J. D. Surratt, R. Szmigielski and J. Wildt, *Atmos. Chem. Phys.*, 2009, **9**, 5155-5236.
18. A. Ylisirniö, A. Buchholz, C. Mohr, Z. Li, L. Barreira, A. Lambe, C. Faiola, E. Kari, T. Yli-Juuti, S. A. Nizkorodov, D. R. Worsnop, A. Virtanen and S. Schobesberger, *Atmos. Chem. Phys. Discuss.*, 2019, **2019**, 1-29.
19. F. Bianchi, T. Kurten, M. Riva, C. Mohr, M. P. Rissanen, P. Roldin, T. Berndt, J. D. Crounse, P. O. Wennberg, T. F. Mentel, J. Wildt, H. Junninen, T. Jokinen, M. Kulmala, D. R. Worsnop, J. A. Thornton, N. Donahue, H. G. Kjaergaard and M. Ehn, *Chem. Rev.*, 2019, **119**, 3472-3509.
20. M. S. Claflin, J. E. Krechmer, W. W. Hu, J. L. Jimenez and P. J. Ziemann, *ACS Earth Space Chem.*, 2018, **2**, 1196-1210.
21. L. Chen, Y. Huang, Y. Xue, Z. Shen, J. Cao and W. Wang, *Atmos. Chem. Phys.*, 2019, **19**, 4075-4091.
22. L. Vereecken, A. R. Rickard, M. J. Newland and W. J. Bloss, *Physical Chemistry Chemical Physics*, 2015, **17**, 23847-23858.
23. Y. Zhao and D. G. Truhlar, *Theor. Chem. Acc.*, 2008, **120**, 215-241.
24. H. S. Yu, X. He and D. G. Truhlar, *J. Chem. Theory Comput.*, 2016, **12**, 1280-1293.
25. S. Grimme, *Journal of Chemical Physics*, 2006, **124**.
26. S. Grimme, J. Antony, S. Ehrlich and H. Krieg, *Journal of Chemical Physics*, 2010, **132**.
27. L. Goerigk and S. Grimme, *Physical Chemistry Chemical Physics*, 2011, **13**, 6670-6688.
28. X. Xu, I. M. Alecu and D. G. Truhlar, *J. Chem. Theory Comput.*, 2011, **7**, 1667-1676.
29. Y. Zhao and D. G. Truhlar, *Acc. Chem. Res.*, 2008, **41**, 157-167.
30. J. Zheng, Y. Zhao and D. G. Truhlar, *J. Chem. Theory Comput.*, 2009, **5**, 808-821.
31. M. Balaganesh and B. Rajakumar, *J. Phys. Chem. A*, 2012, **116**, 9832-9842.
32. B. Long, J. L. Bao and D. G. Truhlar, *Journal of the American Chemical Society*, 2016, **138**, 14409-14422.
33. Y. Fang, F. Liu, V. P. Barber, S. J. Klippenstein, A. B. McCoy and M. I. Lester, *Journal of Chemical Physics*, 2016, **144**.
34. S. J. Klippenstein, *Proc. Combust. Inst.*, 2017, **36**, 77-111.
35. R. Chow, D. K. W. Mok, E. P. F. Lee and J. M. Dyke, *Physical Chemistry Chemical Physics*, 2016, **18**, 30554-30569.
36. M. J. Frisch, G. W. Trucks, H. B. Schlegel, G. E. Scuseria, M. A. Robb, J. R. Cheeseman, G. Scalmani, V. Barone, G. A. Petersson, H. Nakatsuji, X. Li, M. Caricato, A. V. Marenich, J. Bloino, B. G. Janesko, R. Gomperts, B. Mennucci, H. P. Hratchian, J. V. Ortiz, A. F. Izmaylov, J. L. Sonnenberg, D. Williams-Young, F. Ding, F. Lipparini, F. Egidi, J. Goings, B. Peng, A. Petrone, T. Henderson, D. Ranasinghe, V. G. Zakrzewski, J. Gao, N. Rega, G. Zheng, W. Liang, M. Hada, M. Ehara, K. Toyota, R. Fukuda, J. Hasegawa, M. Ishida, T. Nakajima, Y. Honda, O. Kitao, H. Nakai, T. Vreven, K. Throssell, J. A. Montgomery, Jr., J. E. Peralta, F. Ogliaro, M. J. Bearpark, J. J. Heyd, E. N. Brothers, K. N. Kudin, V. N.

Staroverov, T. A. Keith, R. Kobayashi, J. Normand, K. Raghavachari, A. P. Rendell, J. C. Burant, S. S. Iyengar, J. Tomasi, M. Cossi, J. M. Millam, M. Klene, C. Adamo, R. Cammi, J. W. Ochterski, R. L. Martin, K. Morokuma, O. Farkas, J. B. Foresman and D. J. Fox, Gaussian Inc., Walling Ford, CT, United States2016.
37. E. E. Greenwald, S. W. North, Y. Georgievskii and S. J. Klippenstein, *J. Phys. Chem. A*, 2007, **111**, 5582-5592.
38. J. Troe and V. G. Ushakov, *Journal of Chemical Physics*, 2012, **136**.
39. Y. Georgievskii and S. J. Klippenstein, *Journal of Chemical Physics*, 2005, **122**.
40. M. Alipour, *Chem. Phys. Lett.*, 2016, **644**, 163-166.
41. W. L. Ting, Y. H. Chen, W. Chao, M. C. Smith and J. J. M. Lin, *Physical Chemistry Chemical Physics*, 2014, **16**, 10438-10443.
42. A. C. Rousso, N. Hansen, A. W. Jasper and Y. G. Ju, *Physical Chemistry Chemical Physics*, 2019, **21**, 7341-7357.
43. J. Zheng, S. Zhang, B. J. Lynch, J. C. Corchado, Y.-Y. Chuang, P. L. Fast, W.-P. Hu, Y. P. Liu, G. C. Lynch, K. A. Nguyen, C. F. Jackels, A. Fernandez-Ramos, B. A. Ellingson, V. S. Melissas, J. Villà, I. Rossi, E. L. Coitino, J. Pu, T. V. Albu, R. Steckler, B. C. Garrett, A. D. Isaacson and D. G. Truhlar, Department of Chemistry and Supercomputing Institute, University of Minnesota, Minneapolis, Minnesota 55455, 2010 edn., 2010.
44. R. Chow, M. Ng, D. K. W. Mok, E. P. F. Lee and J. M. Dyke, *J. Phys. Chem. A*, 2014, **118**, 2040-2055.
45. J. L. Bao, J. Zheng and D. G. Truhlar, *Journal of the American Chemical Society*, 2016, **138**, 2690-2704.
46. J. Zheng, J. L. Bao, R. Meana-Pañeda, S. Zhang, B. J. Lynch, J. C. Corchado, Y.-Y. Chuang, P. L. Fast, W.-P. Hu, Y. P. Liu, G. C. Lynch, K. A. Nguyen, C. F. Jackels, A. Fernandez-Ramos, B. A. Ellingson, V. S. Melissas, J. Villà, I. Rossi, E. L. Coitiño, J. Pu, T. V. Albu, A. Ratkiewicz, R. Steckler, B. C. Garrett, A. D. Isaacson and D. G. Truhlar, Department of Chemistry and Supercomputing Institute, University of Minnesota, Minneapolis, Minnesota 55455, 2010 edn., 2017.
47. National Oceanic and Atmospheric Administration, National Aeronautics Space Administration and United Airforce, US Standard Atmosphere, 1976, Wasington D.C.
48. P. Zhang, S. J. Klippenstein, H. Y. Sun and C. K. Law, *Proc. Combust. Inst.*, 2011, **33**, 425-432.
49. T. V. T. Mai, M. V. Duong, H. T. Nguyen, K. C. Lin and L. K. Huynh, *Chem. Phys. Lett.*, 2018, **706**, 280-284.
50. J. R. Barker, N. F. Ortiz, J. M. Preses, L. L. Lohr, A. Maranzana, P. J. Stimac, T. L. Nguyen and T. J. D. Kumar, MultiWell Program Suite, version 2019, http://aoss-research.engin.umich.edu/multiwell/ Accessed 5 July, 2019.
51. Y.-T. Su, Y.-H. Huang, H. A. Witek and Y.-P. Lee, *Science*, 2013, **340**, 174-176.
52. T. J. Lee and P. R. Taylor, *Int. J. Quantum Chem.*, 1989, 199-207.
53. L. Chen, Y. Huang, Y. Xue, J. Cao and W. Wang, *J. Phys. Chem. A*, 2017, **121**, 6981-6991.
54. A. Fernandez-Ramos, B. A. Ellingson, B. C. Garret and D. G. Truhlar, *Reviews in Computational Chemistry*, Wiley-VCH, Hoboken, NJ, 2007.
55. A. Fernandez-Ramos, J. A. Miller, S. J. Klippenstein and D. G. Truhlar, *Chem. Rev.*, 2006, **106**, 4518-4584.
56. B. C. Garrett, D. G. Truhlar, R. S. Grev and A. W. Magnuson, *Journal of Physical Chemistry*, 1980, **84**, 1730-1748.
57. C. J. Percival, O. Welz, A. J. Eskola, J. D. Savee, D. L. Osborn, D. O. Topping, D. Lowe, S. R. Utembe, A. Bacak, G. McFiggans, M. C. Cooke, P. Xiao, A. T. Archibald, M. E. Jenkin, R. G. Derwent, I. Riipinen, D. W. K. Mok, E. P. F. Lee, J. M. Dyke, C. A. Taatjes and D. E. Shallcross, *Faraday Discuss.*, 2013, **165**, 45-73.
58. M. M. Kabanda and K. R. N. Serobatse, *J. Sulfur Chem.*, 2018, **39**, 23-46.
59. E. Papajak, J. J. Zheng, X. F. Xu, H. R. Leverentz and D. G. Truhlar, *J. Chem. Theory Comput.*, 2011, **7**, 3027-3034.

60. P. A. Feiner, W. H. Brune, D. O. Miller, L. Zhang, R. C. Cohen, P. S. Romer, A. H. Goldstein, F. N. Keutsch, K. M. Skog, P. O. Wennberg, T. B. Nguyen, A. P. Teng, J. DeGouw, A. Koss, R. J. Wild, S. S. Brown, A. Guenther, E. Edgerton, K. Baumann and J. L. Fry, *J. Atmos. Sci.*, 2016, **73**, 4699-4710.
61. A. Novelli, K. Hens, C. T. Ernest, M. Martinez, A. C. Nolscher, V. Sinha, P. Paasonen, T. Petaja, M. Sipila, T. Elste, C. Plass-Dulmer, G. J. Phillips, D. Kubistin, J. Williams, L. Vereecken, J. Lelieveld and H. Harder, *Atmos. Chem. Phys.*, 2017, **17**, 7807-7826.
62. M. A. H. Khan, W. C. Morris, M. Galloway, B. A. Shallcross, C. J. Percival and D. E. Shallcross, *Int. J. Chem. Kinet.*, 2017, **49**, 611-621.